Acta Crystallographica Section B
Structural Science
ISSN 0108-7681

From six- to five-coordinated Sb^{III} in $[(CH_3)_3PH]_3[Sb_2Cl_9]$: transition pathways from single-crystal X-ray diffraction

Anna Gagor,[a]* Maciej Wojtaś,[b] Adam Pietraszko[a] and Ryszard Jakubas[b]

[a]W. Trzebiatowski Institute of Low Temperature and Structure Research PAS, PO Box 1410, 50-950 Wrocław, Poland, and [b]Faculty of Chemistry, University of Wrocław, Joliot–Curie 14, 50-383 Wrocław, Poland

Correspondence e-mail: a.gagor@int.pan.wroc.pl

Received 27 June 2008
Accepted 25 August 2008

$[(CH_3)_3PH]_3[Sb_2Cl_9]$ experiences four phase transitions which were found by means of calorimetry, thermogravimetry and X-ray diffraction. The crystal structure was solved in the space group $P6_3/mmc$ at 382 K (phase I), $Pnam$ at 295 K (phase II) and $Pna2_1$ at 175 K (phase V). We observed an unusual increase in symmetry from the monoclinic to the orthorhombic form at the IV→V transition. The parent hexagonal high-temperature phase I consists of highly disordered $[(CH_3)_3PH]^+$ cations and $[Sb_2Cl_9]^{3-}$ anions with an octahedral environment of Sb^{III}. The transition from phases I to II is associated with the ordering of $[(CH_3)_3PH]^+$ cations. Moreover, the successive transformations from phases I to V are related to the change in the arrangement of Cl atoms in $[Sb_2Cl_9]^{3-}$ anions from the discrete 'face-sharing bioctahedra' (phase I) to two corner-sharing square pyramids. A mechanism for the phase transitions is proposed. It is observed that weak C—H···Cl interactions are responsible for the structure arrangement in low-temperature phases.

1. Introduction

The physical properties of the alkylammonium halogenoantimonates(III) and halogenobismuthates(III) with the general formula $R_aM_bX_{(3b+a)}$ (where R stands for organic cation; M stands for Sb, Bi; and X = Cl, Br, I) have attracted considerable attention in the last decade (Sobczyk *et al.*, 1997; Jakubas & Sobczyk, 1990; Iwata & Ishibashi, 1992; Iwata *et al.*, 1999). Over a dozen crystals belonging to this family reveal ferroelectric properties. Such materials are of interest for practical applications due to their piezoelectric and nonlinear optical properties (Ravez, 2000; Scott, 2000). The halogenoantimonates(III) and halogenobismuthates(III) are characterized by a rich diversity in the form of the anionic substructure. The interesting feature of this family of crystals is that the ferroelectric properties are limited to the $R_5M_2X_{11}$, $R_3M_2X_9$ and RMX_4 chemical stoichiometries. Within the $R_5M_2X_{11}$ group synthesized so far, all salts exhibit ferroelectric properties. They contain discrete bioctahedral units Bi_2X_{11} in the crystal lattice (Carpentier *et al.*, 1997; Jóźków *et al.*, 2001). On the other hand, the $R_3M_2X_9$ family was found to possess four different anionic subunits. The MX_6 octahedra can share corners, edges or faces, forming infinite one-dimensional chains (type *a*) (Jakubas *et al.*, 1986), two-dimensional layers (*b*) (Kallel & Bats, 1985), discrete bioctahedral units (*c*) (Chabot & Parthé, 1978) and discrete tetramers (*d*) (Aurivillius & Stälhandske, 1978). Ferroelectric properties were found only in the *b*-type of $R_3M_2X_9$ compounds.

In the search for new polar materials we have extended our studies on the halogenoantimonates(III) and halogenobismuthates(III) embedded in the anionic substructure of

alkylphosphonium cations. We have systematically studied four tetramethylphosphonium analogues crystallizing in the $R_3M_2X_9$ composition and characterized by the *c*-type of anionic substructure (face-sharing discrete bioctahedra). All the $[P(CH_3)_4]_3M_2X_9$ analogues studied so far have been found to exhibit ferroic/ferroelastic properties at low temperatures (Wojtaś & Jakubas, 2004; Wojtaś *et al.*, 2004). Some of the phases also exhibit pyroelectric/polar properties with irreversible spontaneous polarization, which is unexpectedly large (of the order of 10^{-4} C m^{-2}) and characteristic of a 'weak' ferroelectric. On the other hand, the incorporation of dipolar trimethylphosphonium cations in the anionic matrix may be helpful in generating polar properties in this class of compounds.

A new trimethylphosphonium analogue, $[(CH_3)_3PH]_3[Sb_2Cl_9]$, has been synthesized and structurally characterized in its various polymorphic phases. The phase situation in this compound has been described by means of the thermal methods differential scanning calorimetry (DSC), thermogravimetric analysis (TGA) and differential thermal analysis (DTA). The ferroelastic (ferroic) properties of this compound are analysed, and a mechanism for the phase transitions is proposed.

2. Synthesis

The trimethylphosphine was solubilized in concentrated HCl (46%) and then mixed in stoichiometric ratio with Sb_2O_3 solubilized in concentrated HCl. The colourless, pseudo-hexagonal plate-shaped crystals of $[(CH_3)_3PH]_3[Sb_2Cl_9]$ were obtained by slow evaporation of this solution.

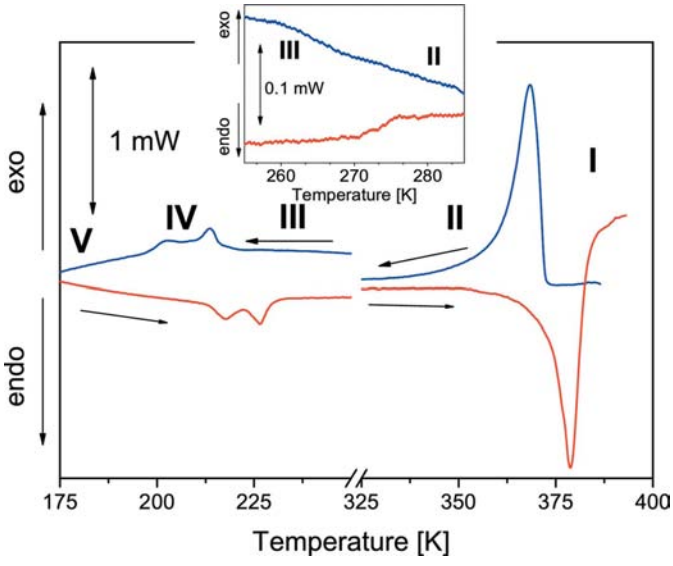

Figure 1
DSC curves of the $[(CH_3)_3PH]_3[Sb_2Cl_9]$ crystal for the cooling and heating runs (10 K min^{-1}). The inset shows the DSC curves in the vicinity of 272 K.

3. Thermal analysis

DSC measurements on powdered samples were carried out using a Perkin Elmer DSC-7 in the temperature range 100–395 K with a scan rate of 10 K min^{-1}.

TGA and DTA were made on a Setaram SETSYS 16/18 instrument in a nitrogen atmosphere. The sample mass was 11.944 mg, the heating rate 2 K min^{-1}, and the temperature range 300–550 K.

Fig. 1 presents the results of DSC measurements. Starting from room temperature, on the cooling scan, $[(CH_3)_3PH]_3[Sb_2Cl_9]$ experiences three phase transitions (PTs). The first one, from phases II to III, is manifested only as a subtle deflection of the baseline and takes place at 272 K. Next, two successive phase transitions, at 216 and 206 K, are manifested as peaks. The lower-temperature one is slightly widened, which suggests that the IV→V transformation, characterized by a small enthalpy effect, is of the mixed continuous–discontinuous type. The temperature hysteresis for the IV→V and III→IV phase transitions amounts to 11 K and 9 K, respectively. The transformation from phases III to II takes place at 272 K. The lack of temperature hysteresis as well as the shape of the thermal anomaly indicate a continuous character of this PT. On further heating, the sample at 375 K undergoes another PT of the discontinuous type. On cooling, this transformation is shifted down to 372 K. All these phase transitions are reversible.

It is important to note that the I↔II phase transition is characterized by a large change of entropy, $\Delta S \simeq 18$ J K^{-1} mol^{-1}.

In Fig. 2 the TGA and DTA curves are presented. At 376 K a endothermic anomaly manifested as a peak is observed. It is related to the II→I phase transition recorded previously in DSC measurements. When the temperature exceeds 420 K, the continuous process of sample decomposition starts. It is related to a huge endothermic effect. A slight mass loss (of the order of 1.5%) is visible already at 360 K, *i.e.* in phase II.

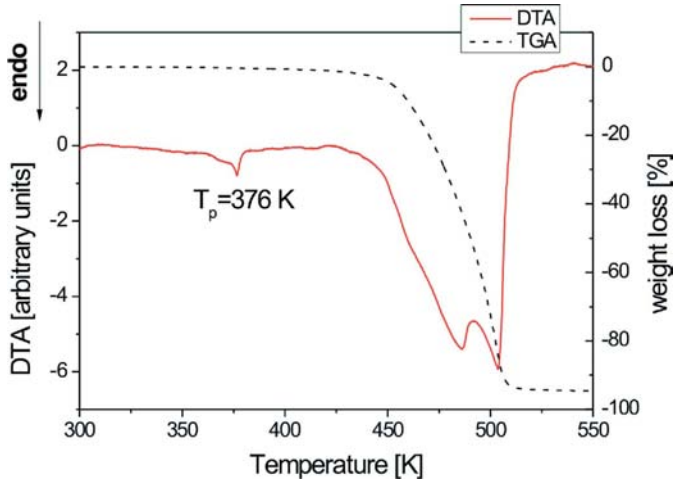

Figure 2
Simultaneous TGA and DTA scans for $[(CH_3)_3PH]_3[Sb_2Cl_9]$. The scans were performed in flowing nitrogen with a ramp rate of 2 K min^{-1} (selected single crystals, nitrogen atmosphere, flow rate 1 dm^3 h^{-1}).

Table 1
Crystal data, experimental details and structure refinement results for $[(CH_3)_3PH]_3[Sb_2Cl_9]$.

Phase	V	II	I
Crystal data			
Chemical formula	$3C_3H_{10}P{\cdot}Cl_5Sb{\cdot}Cl_4Sb$	$3C_3H_{10}P{\cdot}Cl_9Sb_2$	$C_{18}H_{60}Cl_{18}P_6Sb_4$
Temperature (K)	175 (2)	295 (2)	382 (2)
Cell setting, space group	Orthorhombic, $Pna2_1$	Orthorhombic, $Pnam$	Hexagonal, $P6_3/mmc$
M_r	793.79	793.81	1587.67
a, b, c (Å)	14.842 (3), 9.3475 (19), 21.624 (4)	15.070 (3), 9.3026 (19), 22.008 (4)	9.1910 (13), 9.1910 (13), 22.011 (4)
V (Å^3)	3000.1 (10)	3085.3 (11)	1610.3 (4)
Z	4	4	1
D_x (Mg m^{-3})	1.757	1.709	1.637
Radiation type	Mo $K\alpha$	Mo $K\alpha$	Mo $K\alpha$
μ (mm^{-1})	2.76	2.68	2.57
Crystal form, colour	Rectangular prism, colourless	Rectangular prism, colourless	Rectangular prism, colourless
Crystal size (mm)	0.25 × 0.17 × 0.17	0.25 × 0.17 × 0.17	0.25 × 0.17 × 0.17
Data collection			
Diffractometer	KM4 CCD	KM4 CCD	KM4 CCD
Data collection method	$\Delta\omega$	$\Delta\omega$	$\Delta\omega$
Absorption correction	Multi-scan†	Multi-scan†	Multi-scan†
T_{min}	0.56	0.58	0.57
T_{max}	0.63	0.64	0.64
No. of measured, independent and observed reflections	54 675, 16 806, 10 215	36 684, 4156, 2130	6828, 680, 312
Criterion for observed reflections	$I>2\sigma(I)$	$I>2\sigma(I)$	$I>2\sigma(I)$
R_{int}	0.041	0.037	0.031
θ_{max} (°)	43.9	29.4	26.7
Refinement			
Refinement on	F^2	F^2	F^2
$R[F^2>2\sigma(F^2)]$, $wR(F^2)$, S	0.026, 0.061, 0.94	0.031, 0.107, 1.04	0.053, 0.169, 0.99
No. of reflections	16 806	4156	680
No. of parameters	275	129	34
Weighting scheme	$w = 1/[\sigma^2(F_o^2) + (0.028P)^2]$, where $P = (F_o^2 + 2F_c^2)/3$	$w = 1/[\sigma^2(F_o^2) + (0.0347P)^2 + 1.255P]$, where $P = (F_o^2 + 2F_c^2)/3$	$w = 1/[\sigma^2(F_o^2) + (0.070P)^2 + 2.750P]$, where $P = (F_o^2 + 2F_c^2)/3$
$(\Delta/\sigma)_{max}$	0.027	0.002	0.015
$\Delta\rho_{max}$, $\Delta\rho_{min}$ (e Å^{-3})	1.32, −1.31	0.56, −0.54	0.31, −0.43

† Based on symmetry-related measurements.

4. Crystal structure

4.1. X-ray data collection and processing

A single-crystal X-ray data collection was performed on a Kuma KM4 CCD diffractometer with graphite-monochromated Mo $K\alpha$ radiation. Small single-domain crystals were carefully selected and checked for twinning. A crystal of approximate dimensions 0.25 × 0.17 × 0.17 (mm) was mounted with epoxy glue at the tip of quartz fibre and used for data collection in the ferroelastic phases at 295 and 175 K. For the measurements of the paraelastic phase at 382 K the same sample was put at the tip of quartz capillary to prevent the crystal from sublimation at high temperature. Thermal evolution of lattice parameters was measured for two samples from 100 to 385 K with a step of 10–15 K and cooling/heating rates of 2 and 2.5 K min^{-1} for the first and the second sample, respectively. Lattice parameters were obtained by a least-square fit to 150 reflections. An open-flow nitrogen cryosystem (Oxford Cryosystem, covering the temperature range 90–320 K) was used for experiments from 295 to 100 K, while a simple high-temperature attachment with hot-air flow (Kuma Diffraction, covering the temperature range 300–770 K) was used for the experiments at temperatures ranging between 295 and 385 K.

CrysAlis software (Oxford Diffraction, 2007) was used for data processing. An empirical absorption correction was applied using spherical harmonics implemented in the *SCALE3 ABSPACK* scaling algorithm. The structure was solved by direct methods and refined by the full-matrix least-squares method by means of the *SHELX97* program package (Sheldrick, 2008). The valence of antimony has been calculated from the refined structure models using the bond-valence method (Brown, 1996). More details on data collection and reduction are given in Table 1.

The structure of the high-temperature prototype phase I was solved in the space group $P6_3/mmc$, as suggested by averaging of reflection intensities. However, the H atoms were not localized due to the orientational disorder of $[(CH_3)_3PH]^+$ cations observed in this phase. The symmetry determination of the room-temperature phase II was also straightforward since reflection intensity averaging led to two possible space groups, $Pnma$ and $Pna2_1$. Refinement of the structure in $Pna2_1$ led to high atomic displacement parameters and large correlation matrix elements (>0.93) between positional and atomic

displacement parameters of the Sb and Cl atoms. Also, no pyroelectric effect was observed at room temperature (Wojtaś *et al.*, 2008). The structure was successfully solved in the non-standard setting *Pnam* of the centrosymmetric group *Pnma* to keep the cell choice of phase I. Due to the twinning accompanying the symmetry change from orthorhombic to monoclinic, the structure of phase III was not solved. Averaging done for the main twin component (60% indexed peaks) as well as careful analysis of reciprocal-space reconstructions and systematic absences led to only one possible space group ($P2_1/a$ at 240 K). The twinning resulted in splitting of the diffraction peaks in the c^* direction and partial overlapping of diffraction peaks from different twin domains. Several attempts, for different crystals, were made to solve the structure. An isotropic refinement, based on the intensity data prepared in *CrysAlisPro* (software which provides the tools for simultaneous indexing of different twin components), resulted in a very poor R factor ($\simeq$ 23%). Refinement of the structure from powder data (on the basis of the structure model from phase II) was also unsuccessful. The structure determination of phase IV was not performed for the same reasons. Additionally, the satellites resulting from modulation with wavevector $q \simeq 0.33c^*$ (c = 21.98 Å) were overlapped partially with the main peaks which made it impossible to determine the accurate value of the wavevector and the structure (14% of all measured reflections were completely overlapped, whereas only 0.35% were completely separated). The symmetry of phase IV was found to be monoclinic with space group $P2_1/a$ for main reflections; $P2_1/a$ symmetry was also found for the 3c superstructure ($c' \simeq$ 66 Å). The phase transition from phases IV to V was associated with a symmetry increase to the orthorhombic $Pna2_1$ space group. Despite the fact that averaging suggested two possible space groups (centrosymmetric *Pnam* and non-centrosymmetric $Pna2_1$), the latter one was chosen since the polar nature of phase V was confirmed by pyroelectric measurements (Wojtaś *et al.*, 2008).

Some H atoms were placed in calculated positions and others were located in difference maps. In phase II, apart from disordered atoms, the H atoms bound to the C atoms were included in geometric positions and treated as riding atoms. The attempts to refine the positions of the H atoms involved in hydrogen bonds failed since such a treatment resulted in a high variability of bond angles in methyl groups, even though bond and angle restraints were used. In phase V, the positions of H atoms from methyl groups interacting with Cl^- ions by hydrogen bonds were taken from the difference-Fourier maps and refined with restraints, whereas the positions of the remaining H atoms were placed in geometrically idealized positions and included as riding atoms. In both phases, H atoms bound to P atoms were taken from difference-Fourier maps, refined separately and then fixed. The authors were aware that the determination of H-atom positions in the presence of antimony may be considered questionable; nevertheless, the results obtained showed the bonding in $[(CH_3)_3PH]_3[Sb_2Cl_9]$ in phases II and V.

4.2. Thermal evolution of lattice parameters

To verify the structure transformations disclosed by DSC, the temperature evolution of lattice parameters and angle β between 100 and 380 K were measured for two different crystals. Figs. 3 and 4 give the values of tje monoclinic β angle and the lattice parameters *versus* temperature which are given according to the orthorhombic cell choice of the room-temperature phase. The character of the changes in the lattice parameters confirms the presence of four structural phase transitions at 370, 275, 220 and 200 K, on cooling. The high-temperature prototype phase was found to be hexagonal with $P6_3/mmc$ symmetry. Below 370 K the crystal structure adopts an orthorhombic system with the *Pnam* space group. At 275 K the symmetry lowers to the monoclinic $P2_1/a$. This transition is associated with twinning of the crystal structure. Next, below 220 K, the modulated monoclinic phase is stabilized with the modulation vector in the c direction. This phase transition is associated with a significant expansion of the crystal along c and a much smaller one along the b axis of 0.1 and 0.025 Å at

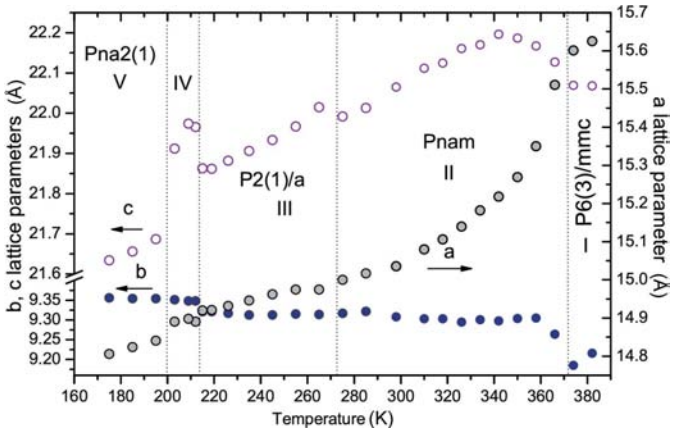

Figure 3
Temperature evolution of lattice parameters in $[(CH_3)_3PH]_3[Sb_2Cl_9]$. Standard deviations are comparable to the points marked in the figure.

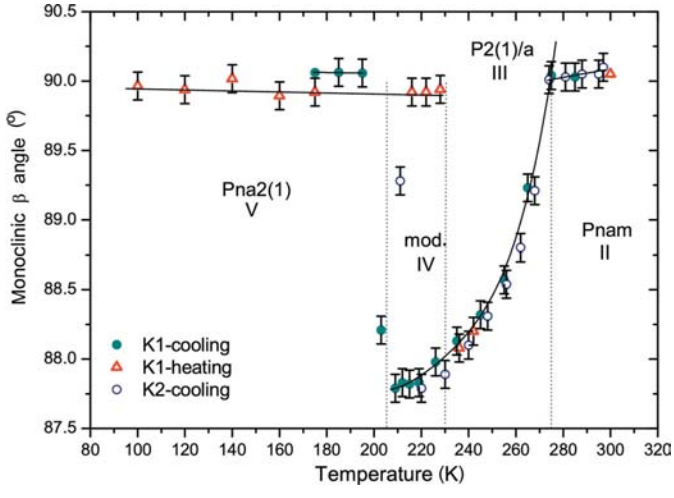

Figure 4
The temperature evolution of monoclinic β angle in $[(CH_3)_3PH]_3[Sb_2Cl_9]$ measured for two samples (K1 and K2) in cooling and heating runs.

the transition point, respectively. At 200 K, the crystal symmetry increases unexpectedly to orthorhombic $Pna2_1$. The monoclinic distortion of $\simeq 2^\circ$ observed at 205 K vanishes below 200 K. The phase transformation is also accompanied by a dramatic contraction of the crystal along the *c* direction by *ca* 0.31 Å.

4.3. Phase I

At high temperatures, $[(CH_3)_3PH]_3[Sb_2Cl_9]$ adopts a hexagonal system with the $P6_3/mmc$ space group. The asymmetric unit of phase I contains two one-half $[(CH_3)_3PH]^+$ cations, denoted as MP1 and MP2, along with one Sb and two Cl atoms which form the symmetric $[Sb_2Cl_9]^{3-}$ anion with the mirror plane imposed at the mid-point between two Sb atoms and a threefold axis parallel to the Sb1–Sb1′ direction. In this way, the $[Sb_2Cl_9]^{3-}$ bioctahedron of D_{3h} symmetry is produced (see Fig. 5).

The anionic component can be described as two $SbCl_6$ face-sharing octahedra. Bond angles in the individual $SbCl_6$ octahedra deviate from ideal octahedral angles [*cis* angles range from 81.137 (8) to 94.06 (7)°]. All bond distances and angles of the $[Sb_2Cl_9]^{3-}$ bioctahedron, however, are comparable to those observed in similar anions in bismuth and antimony halide chemistry: in $[(CH_3)_3PH]_3[Sb_2Cl_9]$ Sb—Cl11 = 2.421 (4) Å and Sb—Cl1 = 2.9098 (3) Å while in the paraelectric phase of $[(CH_3)_3NH]_2Sb_2Cl_9$ the average $Sb—Cl_{terminal}$ distance is 2.427 Å and $Sb—Cl_{bridging}$ = 3.057 Å (Bujak & Zaleski, 2001). The important distances and bond angles are summarized in the supplementary materials[1].

The cations fill large holes between the anions. In the $P6_3/mmc$ phase there are two symmetry-independent $[(CH_3)_3PH]^+$ cations, both of which are disordered. Fig. 6 shows the structure of disordered $[(CH_3)_3PH]^+$ cations in the high-temperature phase. The orientation disorder of the MP1 group merely drives from the fact that the site point-group symmetry of MP1 is higher than the molecular C_{3v} point group of the $[(CH_3)_3PH]^+$ cation. The P1 atom from MP1 resides at the $\bar{6}m2$ (D_{3h}) position and thus MP1 is disordered over six different orientations about the sixfold rotation-inversion axis and twofold axis. Since the P1—C12 bond is located along the sixfold axis the P1—H bond is disordered over six positions. The P2 atom from MP2 is located at the $3m.$ (C_{3v}) site with the P2—C22 bond located along the threefold axis so that the MP2 cation along with the P2—H bond are disordered over three positions. The average P1—C distance in the first cation is identical in the error limit to the similar distance P2—C in the other one [1.76 (4) *versus* 1.75 (2) Å]. The details of the geometry of the $[(CH_3)_3PH]^+$ cations are given in the supplementary materials. Besides orientational disorder, both cations exhibit considerable thermal motion. Nevertheless, the equivalent displacement parameter U_{eq} of the P2 atom is too low in comparison with the U_{eq} of neighbouring C21 and C22 atoms, probably pointing to some unresolved disorder. Further efforts to represent the disorder of the MP2 cation are not warranted, however, since Fourier maps do not show any additional residuals in the proximity of C atoms. The disorder and large thermal motion of the cations in phase I are probably the result of the lack of directional bonding and large volume available in the structure.

4.4. Phase II

In phase II there are three independent terminal and three bridging chlorine positions. Two bridging Cl2 and Cl3 positions are statistically occupied, with a site-occupation factor of 0.5. This leads to the deformation of the inorganic part, changing the Sb arrangement. Atom Sb1 is strongly bonded to three terminal Cl atoms with an average bond length of 2.476 Å, and weakly bonded to the remaining bridging atoms which display an anisotropy in distance length. The Sb1—Cl1 distance is 2.849 (2) Å, while the Sb1—Cl2, Sb1—Cl3 distances are 2.701 (2) and 2.721 (2) Å, respectively. Two

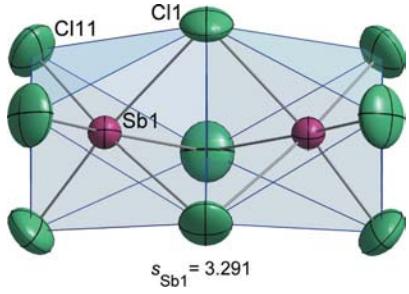

Figure 5
$[Sb_2Cl_9]^{3-}$ bioctahedron in the crystal structure of the high-temperature prototype phase I. The bond-valence sum *s* for Sb1 coordination is given. Displacement ellipsoids have been drawn at the 15% probability level for clarity.

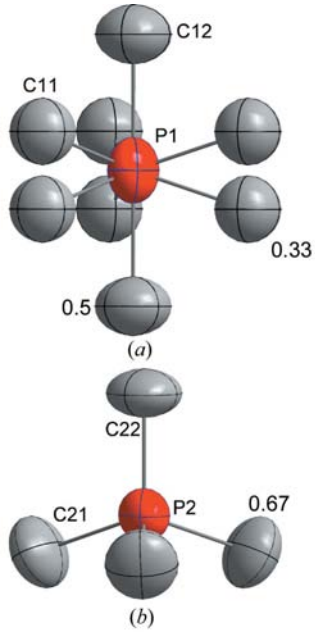

Figure 6
Structure of disordered $[(CH_3)_3PH]^+$ groups (*a*) MP1 and (*b*) MP2 in phase I. Displacement ellipsoids have been drawn at the 15% probability level for clarity. The site-occupation factors of carbon positions are given.

[1] Supplementary data for this paper are available from the IUCr electronic archives (Reference: BM5058). Services for accessing these data are described at the back of the journal.

bridging Cl atoms may occupy two equivalent positions generated by a mirror plane imposed in the middle of the Sb—Sb′ distance. These are Cl2 and Cl2′ positions at the distance of 0.8825 (2) Å and Cl3 and Cl3′ at the distance of 0.8431 (2) Å. In this way, the environment of Sb changes from two face-sharing octahedra in phase I to two corner-sharing square pyramids in phase II. These pyramids can switch their orientation state from the vertex at position Cl11 to Cl12. Fig. 7(*a*) shows the average configuration of $[Sb_2Cl_9]^{3-}$ in phase II. Figs. 7(*b*) and (*c*) present the most probable coordination of the Sb atoms. The bond-valence sum (*s*) for both square pyramids is lower than the ideal number of 3 due to the distorted Sb environment. The positions of Cl2′ and Cl3′ are far removed from the Sb1 atom [3.274 (1) and 3.270 (1) Å, respectively] and their contribution to the bond-valence sum is much lower than that of the remaining atoms. We have thus decided not to involve them in the coordination sphere of Sb1. Another possible arrangement (see Fig. 7*d*), which consists of one octahedral and one four-coordinated Sb, is much less probable since the bond-valence sum for four-coordinated Sb is very low (s = 2.5 Å).

The square-pyramidal environment of the Sb^{III} atom is unusual for $R_3M_2X_9$ stoichiometry salts. However, such a coordination is encountered for RMX_4 and R_2MX_5 compounds (Ensinger *et al.*, 1983; Geiser *et al.*, 1990; Wismer & Jacobson, 1974).

Compared with the high-temperature phase I, we observe a slight lengthening of the Sb1—Sb1 distance [3.895 (1) *versus* 3.843 (2) Å] and a corresponding increase in the Sb1—Cl1—Sb1 angle [86.25 (4) *versus* 82.63 (1)°]. The changes affect the volume of the unit cell and result in an increase in the *c* lattice parameter.

Similarly to the high-temperature phase, there are two symmetrically independent $[(CH_3)_3PH]^+$ cations in the crystal structure. However, the number of orientational states which adopt the $[(CH_3)_3PH]^+$ cation is reduced to three (see Fig. 8).

As regards the MP1, the number of orientational states in phase II is reduced to two. The arrangement of the C11 atom in two independent positions [C11*a* and C11*b* at the distance of 0.85 (2) Å] leads to two equivalent orientations of the MP1 group. The observed disorder originates in the statistical distribution of the $Cl2^-$ ion in the $[Sb_2Cl_9]^{3-}$ anion since the MP1 cation interacts with $Cl2^-$ *via* a hydrogen bond. In phase II a hydrogen bond between MP1 and the $Cl2^-$ ion, with a donor–acceptor distance of 3.753 Å and a P1—H1*P*···Cl2 angle of 153°, is created. This interaction is responsible for the site disorder of the MP1 cation. The $Cl2^-$ acceptor statistically occupies two symmetrically equivalent positions which are separated by a distance of 0.882 (6) Å. The jumps of the $Cl2^-$ ion between these two positions change the direction of the P1—H1*P*··· Cl2 bond. As a result, the MP1 cation leans out from the mirror plane in the direction of the P1—H1*P*··· Cl2 bond and adopts two different orientations (see Fig. 9). Thus, the disorder in $[(CH_3)_3PH]_3[Sb_2Cl_9]$ observed in phase II is of a dual nature: the statistical distribution of the $Cl2^-$ ion results in orientational disorder of the MP1 group.

The MP2 cation adopts one state of C_1 symmetry. The group serves to bridge four different anion units by five hydrogen bonds. Namely, three C21—H··· Cl and two C23—H··· Cl bonds (see Table 2), with donor–acceptor distances varying from 3.447 (9) to 3.719 (7) Å. MP2 interacts mainly with two disordered ions ($Cl2^-$ and $Cl3^-$); this interaction is manifested mainly in the high carbon displacement parameters compared with the central P1 atom. The presence of three extra

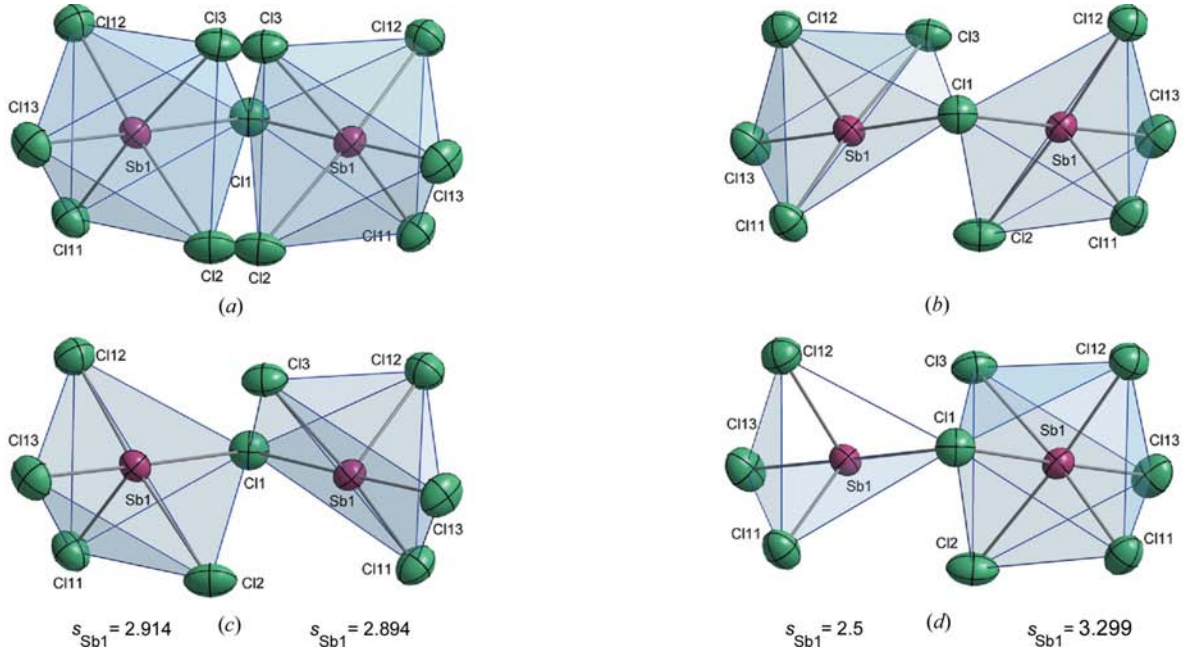

Figure 7
(*a*) Average arrangement, and (*b*)–(*d*) possible configurations of $[Sb_2Cl_9]^{3-}$ anions in the crystal structure of phase II. Displacement ellipsoids have been drawn at the 30% probability level for clarity. The bond-valence sum *s* for different Sb1 coordination is given.

hydrogen bonds, however, preserves the group from significant disorder and stabilizes the cation. Fig. 10 shows the hydrogen bonds between the MP2 cation and the $[Sb_2Cl_9]^{3-}$ anion. The hydrogen-bond geometry is presented in Table 2.

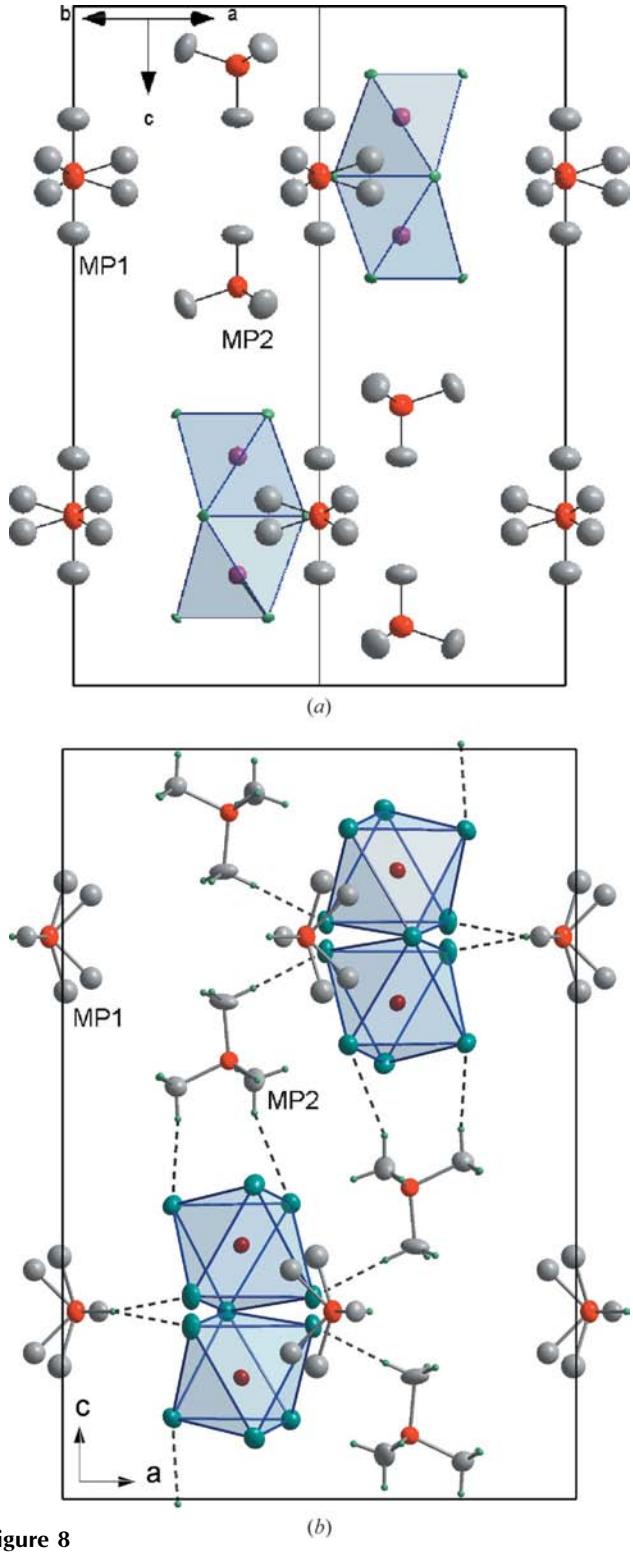

Figure 8
(*a*) The view of the $[(CH_3)_3PH]_3[Sb_2Cl_9]$ hexagonal unit-cell structure in the [110] direction, $T = 382$ K. (*b*) The view of the half unit cell (a, $\frac{1}{2}b$, c) in the [010] direction, showing the orientation of $[(CH_3)_3PH]^+$ groups in phase II, average configuration of $[Sb_2Cl_9]^{3-}$and hydrogen bonds, T = 295 K. Displacement ellipsoids have been drawn at the 20% probability level.

4.5. Phases III and IV

Phase III adopts the monoclinic system with the $P2_1/a$ space group and the lattice parameters at 240 K are a = 14.989, b = 9.323, c = 21.877 Å and β = 91.89°. Despite the fact that attempts to refine the crystal structure failed, we can assume from the requirements of the symmetry that the asymmetric unit of phase III consists of three independent $[(CH_3)_3PH]^+$ groups of C_1 symmetry as well as $[Sb_2Cl_9]^{3-}$ of C_1 symmetry.

Below 220 K the modulated phase IV is stabilized. The systematic absences for the main reflections are characteristic of the $P2_1/a$ space group with lattice parameters a = 14.950, b = 9.350, c = 21.980 Å and β = 90.74° at 211 K. The modulation vector $q \simeq 0.33c^*$ points to the formation of a superstructure with $c \simeq 66$ Å for which $P2_1/a$ symmetry was also found.

4.6. Phase V

The asymmetric unit of phase V consists of three $[(CH_3)_3PH]^+$ cations, denoted later in the text as MP1, MP2 and MP3, and Cl_4—Sb1—Cl1—Sb2—Cl_4 units. Sb1 is strongly bonded to three Cl atoms [Cl11 at 2.4097 (6) Å, Cl12 at 2.5385 (6) Å, Cl13 at 2.4839 (7) Å] and weakly bound to another two Cl atoms [Cl2 at 2.7117 (7) Å, Cl1 at 2.8616 (7) Å], representing a distorted square-pyramidal arrangement. The second metal centre is also strongly bound to three Cl atoms [Cl21 at 2.5802 (6) Å, Cl22 at 2.4041 (6) Å, Cl23 at 2.4944 (7) Å], with an additional relatively strong bond to Cl3 at 2.6833 (7) Å and a weaker linkage to Cl1 at 2.8448 (7) Å. The latter Cl atom forms a bridge to Sb1. Thus, the environment of the Sb1 and Sb2 ions consists of two distorted square pyramids, linked by the bridging chlorine atom Cl1. The apexes of the pyramids are situated at the Cl11 and Cl22 positions. The angle Sb1—Cl1—Sb2, which determines the spatial orientation of pyramids, is 87.096 (8)°. There are also further metal contacts with Cl atoms Sb1···Cl3 at 3.3710 (5) Å and Sb2···Cl2 at 3.3382 (4) Å but they are rather

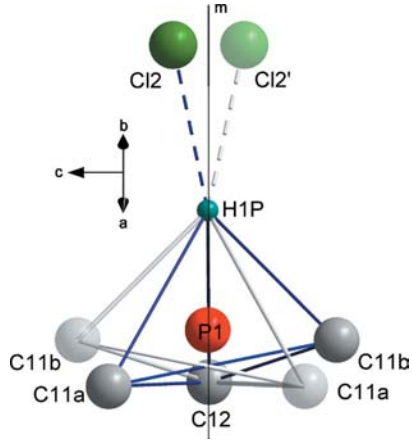

Figure 9
P1—H1*P*···Cl2 hydrogen bond and orientational disorder of the MP1 cation in $[(CH_3)_3PH]_3[Sb_2Cl_9]$ in the orthorhombic phase II.

Table 2
Hydrogen bonds in phases II and V.

D—H···A	$d(D$—H)	d(H···A)	$d(D\cdots A)$	$\angle(DHA)$
Orthorhombic phase (II)				
C21—H21A···Cl2^{ii}	0.96	2.71	3.566 (7)	150
C21—H21B···Cl1^{i}	0.96	2.83	3.719 (7)	154
C21—H21C···Cl3	0.96	2.49	3.447 (9)	171
C23—H23B···Cl11^{iii}	0.95 (2)	2.81 (3)	3.679 (6)	153 (3)
C23—H23C···Cl13^{ii}	0.96 (3)	2.76 (2)	3.699 (6)	165 (4)
P1—H1P···Cl2	1.42	2.43	3.753 (3)	153
P1—H1P···Cl2^{iv}	1.42	2.43	3.753 (3)	153
Orthorhombic phase (V)				
C31—H31A···Cl2^{v}	1.00 (2)	2.69 (2)	3.650 (3)	163 (2)
C31—H31B···Cl1	0.96 (2)	2.81 (2)	3.741 (3)	162 (2)
C21—H21B···Cl1	0.99 (3)	2.74 (3)	3.717 (3)	168 (3)
C21—H21C···Cl3^{vi}	0.88 (3)	2.69 (3)	3.552 (3)	167 (3)
C23—H23B···Cl11^{vii}	0.92 (2)	2.82 (2)	3.613 (3)	145 (2)
C23—H23C···Cl23^{v}	1.01 (2)	2.71 (2)	3.656 (2)	157 (3)
C33—H33C···Cl13^{v}	0.99 (2)	2.72 (3)	3.634 (3)	154 (2)
C33—H33B···Cl21^{viii}	0.96 (2)	2.79 (3)	3.703 (3)	159 (2)
C11—H11B···Cl21^{ix}	1.04 (2)	2.78 (2)	3.714 (3)	149 (2)
P3—H3P···Cl12^{vi}	1.40 (3)	2.81 (3)	3.6571 (10)	117 (1)
P1—H1P···Cl2^{ix}	1.32 (3)	2.64 (3)	3.7679 (11)	142 (1)

Symmetry codes: (i) $x-\frac{1}{2},\frac{1}{2}-y,z$; (ii) $x-\frac{1}{2},-y+\frac{3}{2},z$; (iii) $-x+1,-y+1,-z+2$; (iv) $x,y,-z+\frac{1}{2}$; (v) $x,y+1,z$; (vi) $x-\frac{1}{2},-y+\frac{3}{2},x$; (vii) $-x+\frac{3}{2},y+\frac{1}{2},z+\frac{1}{2}$; (viii) $-x+\frac{3}{2},y+\frac{1}{2},z-\frac{1}{2}$; (ix) $x+\frac{1}{2},-y+\frac{1}{2},z$.

distant to be realistically considered as bonding interactions (Figs. 11 and 12).

The three independent $[(CH_3)_3PH]^+$cations (MP1, MP2 and MP3) are ordered and adopt C_1 symmetry. The MP1 group corresponds to MP1 from phase II whereas MP2 and MP3 correspond to the MP2 group from phase II. An additional MP3 group appears as a consequence of the loss of the . .*m* mirror plane. The cations form quite close hydrogen contacts to Cl^- ions, giving a three-dimensional network of hydrogen bonds in the crystal structure.

The strength of hydrogen bonds does not change significantly compared with phase II. Instead, an additional short contact P3—H3P···Cl12 appears, with a donor–acceptor distance of 3.657 (1) Å. A tendency to improve the geometry of the hydrogen bonds is observed, although the donor–acceptor distances increase in most of the cases (Fig. 13).

5. Conclusions

The phase-transition sequence in $[(CH_3)_3PH]_3[Sb_2Cl_9]$ established on the basis of the calorimetric, X-ray studies and optical observations is illustrated in the diagram below:

$$\underbrace{Pna2_1 \xrightarrow{212\,K} \text{mod.} \xrightarrow{223\,K} P2_1/a \xrightarrow{272\,K} Pnam}_{\text{ferroelastic}} \xrightarrow{375\,K} \underbrace{P6_3/mmm}_{\text{paraelastic}}$$
$$\underbrace{\text{(V)} \qquad \text{(IV)} \qquad \text{(III)} \qquad \text{(II)}}_{\text{ferroelastic}} \qquad \underbrace{\text{(I)}}_{\text{paraelastic}}$$

This crystal exhibits a rich polymorphism in the solid state. The molecular mechanism of the successive phase transitions is explained. The I→II phase transition mechanism is found to be complex. Both 'order–disorder' and 'displacive' contributions should be taken into account. The former contribution is related to the dynamics of the trimethylphosphonium cations which appear to be highly disordered over phase I. The orientational motion of these cations is strictly diminished after crossing the I→II phase-transition temperature. In the high-temperature phase I, the cations labelled as MP1 are distributed over six positions whereas in phase II only two

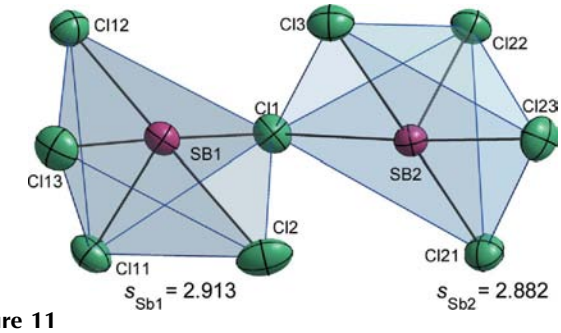

Figure 11
$[Sb_2Cl_9]^{3-}$ anion in the crystal structure of phase V. Displacement ellipsoids have been drawn at the 50% probability level.

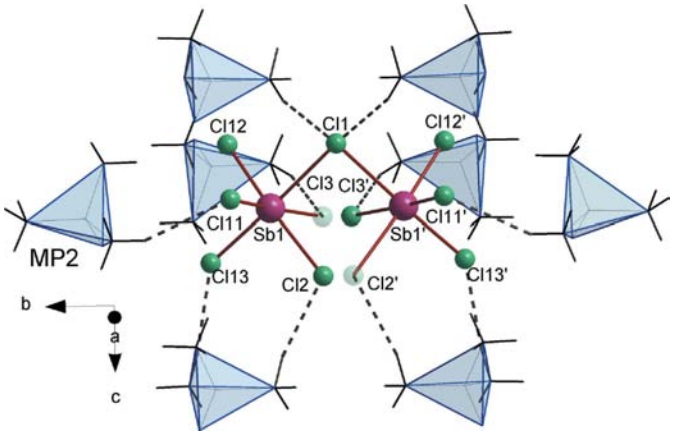

Figure 10
Hydrogen-bond interactions between MP2 cations and $[Sb_2Cl_9]^{3-}$ anions in the crystal structure of phase II.

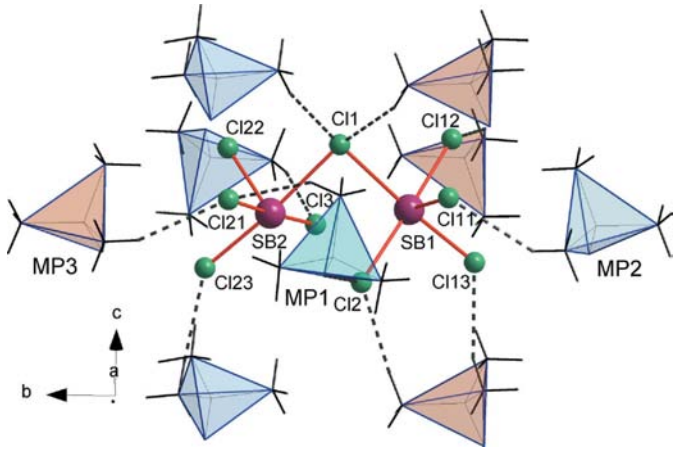

Figure 12
Hydrogen-bond interaction between $[(CH_3)_3PH]^+$ cations and $[Sb_2Cl_9]^{3-}$ anions in the crystal structure of phase V.

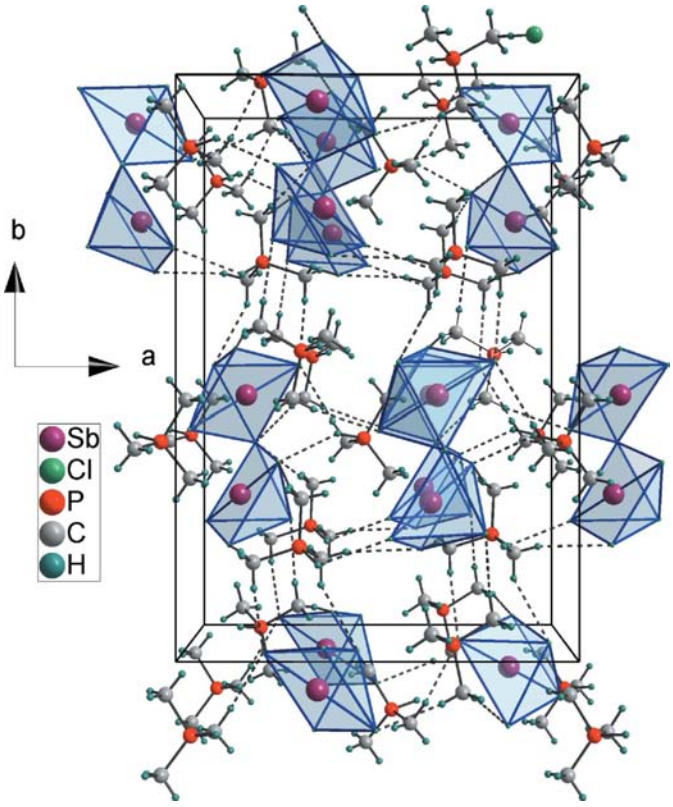

Figure 13
Three-dimensional hydrogen-bond structure in $[(CH_3)_3PH]_3[Sb_2Cl_9]$ in the orthorhombic phase V.

positions are realised. The cations MP2 are distributed over three positions (3*m* site) and in phase II they are fully ordered. The total (three cations) calculated entropy change amounts to: $2R\ln 6/2 + R\ln 3/1 = 27.4$ J (mol K)$^{-1}$ whereas that roughly estimated from the DSC measurements is lower, being about 18 J (mol K)$^{-1}$. Nevertheless, the experimental value of ΔS_{tr} indicates, without any doubts, that the order–disorder contribution dominates the mechanism of phase transition at 375 K. On the other hand, the X–ray analysis of the crystal structure of phases I and II shows that there is an important distortion of the bioctahedral units which is reflected in the shift of the Cl and Sb atoms. It may originate from the 'displacive' contribution to the phase transition. It should be underlined that the distortion of the crystal structure during the ferroic phase transition I→II (hexagonal→orthorhombic symmetry) leads to the ferroelastic order in phase II. In conclusion, for the prototypic ferroeleastic phase transition, the order–disorder contribution is assigned to the dynamics of the organic (cationic) substructure whereas the 'displacive' one is due to the distortion of the anionic substructure.

The mechanism of the lower-temperature transitions II→III, III→IV and IV→V is not as clear as the high-temperature ones. The entropy $\Delta S_{III\rightarrow IV}$ and $\Delta S_{IV\rightarrow V}$ is quite low, below 0.7–0.8 J (mol K)$^{-1}$, which suggests that these transitions are dominated by the 'displacive' mechanism.

Bioctahedral units experience a huge distortion with the successive phase transitions, which is the most intriguing result from the point of view of the crystallochemistry of antimony(III) compounds. The anionic units change from discrete 'face-sharing bioctahedra' (phase I) to two corner-sharing square pyramids. In this case, we have seen a change in the coordination number of the Sb atoms which takes place under constant ambient pressure – this is quite a rare example of such behaviour.

We succeeded in the structure solution of three phases (I, II and V). Further studies should shed light on the crystal structure of the remaining phases (III and IV) and explain in detail the mechanism of related phase transitions in order to obtain the full picture of structural transformations in $[(CH_3)_3PH]_3[Sb_2Cl_9]$.

References

Aurivillius, B. & Stälhandske, C. (1978). *Acta Chem. Scand.* A**32**, 715–719.
Brown, I. D. (1996). *J. Appl. Cryst.* **29**, 479–480.
Bujak, M. & Zaleski, J. (2001). *Cryst. Eng.* **4**, 241–252.
Carpentier, P., Zieliński, P. & Lefebvre, J. (1997). *Z. Phys. B*, **102**, 403–414.
Chabot, B. & Parthé, E. (1978). *Acta Cryst.* B**34**, 645–648.
Ensinger, U., Schwarz, W. & Schmidt, A. (1983). *Z. Naturforsch. B*, **38**, 149–154.
Geiser, U., Wade, E., Wang, H. H. & Williams, J. M. (1990). *Acta Cryst.* C**46**, 1547–1549.
Iwata, M. & Ishibashi, Y. (1992). *Ferroelectrics*, **135**, 283–289.
Iwata, M., Miyashita, A., Orihara, H., Ishibashi, Y., Kuok, M. H., Rang, Z. L. & Ng, S. C. (1999). *Ferroelectrics*, **229**, 233–239.
Jakubas, R., Czapla, Z., Galewski, Z., Sobczyk, L., Żogał, O. & Lis, T. (1986). *Phys. Status Solidi A*, **93**, 449–455.
Jakubas, R. & Sobczyk, L. (1990). *Phase Transitions*, **20**, 163–193.
Jóźków, J., Jakubas, R., Bator, G. & Pietraszko, A. (2001). *J. Chem. Phys.* **114**, 7239–7246.
Kallel, A. & Bats, J. W. (1985). *Acta Cryst.* C**41**, 1022–1024.
Oxford Diffraction (2007). *CrysAlisCCD* and *CrysAlisRED*, including *ABSPACK*. Oxford Diffraction Ltd, Abingdon, Oxford, England.
Ravez, J. (2000). *Chemistry*, **3**, 267–283.
Scott, J. F. (2000). *Ferroelectric Memories*. Berlin, Heidelberg, New York: Springer-Verlag.
Sheldrick, G. M. (2008). *Acta Cryst.* A**64**, 112–122.
Sobczyk, L., Jakubas, R. & Zaleski, J. (1997). *Polish J. Chem.* **71**, 265–300.
Wismer, R. K. & Jacobson, R. A. (1974). *Inorg. Chem.* **13**, 1679–1680.
Wojtaś, M. & Jakubas, R. (2004). *J. Phys. Condens. Matter*, **16**, 7521–7534.
Wojtaś, M., Jakubas, R., Ciunik, Z. & Medycki, W. (2004). *J. Solid State Chem.* **177**, 1575–1584.
Wojtaś, M., Jakubas, R. & Medycki, W. (2008). In preparation.